Supplementary Materials for

Probing optically silent superfluid stripes in cuprates

S. Rajasekaran,* J. Okamoto, L. Mathey, M. Fechner, V. Thampy, G. D. Gu, A. Cavalleri*

*Corresponding author. Email: andrea.cavalleri@mpsd.mpg.de (A.C.); srivats.rajasekaran@mpsd.mpg.de (S.R.)

This PDF file includes:

Materials and Methods
Figs. S1 to S8
References

S1: Methods

Large single crystals of $La_{2-x}Ba_xCuO_4$ with x=9.5%, 11.5% and 15.5% (~4 mm diameter), grown by transient solvent method, were studied here. These crystals belonged to the same batch of samples as reported in an earlier work (*7*), and were cut and polished along the *ac* surface.

Laser pulses at 800-nm wavelength, 100-fs duration and 5 mJ energy were split into 2 parts (99%, 1%) with a beam splitter. The most intense beam was used to generate Terahertz (THz) pulses by optical rectification in $LiNbO_3$ with the tilted pulse front technique(*8*). These THz pulses had energies of ~3 μJ. The pulses were collimated and focused at an incidence angle of 20° onto the samples. The THz pulses were *s*-polarized (i.e., perpendicular to the plane of incidence), corresponding to the direction perpendicular to the Cu-O planes (parallel to the *c* axis, see Fig. S1).

The THz beam spot diameter at the sample position was 2.5 mm, corresponding to a maximum attainable field strength of ~80 kV/cm. The incident field strength was adjusted using a pair of wire grid polarizers.

After reflection from the sample surface, the THz pulse was then electro-optically sampled in a 0.2-mm-thick GaP crystal using the 1% fraction of the 800-nm beam.

This measurement procedure returned the quantity $E_{reflected,sample}(t)$, with *t* being the electro-optic internal time delay. The incident field was measured after reflection from a gold reference, i.e. $E_{reflected,gold}(t)$. The frequency-dependent reflectivity *R* was then derived after computing the Fourier transforms of the time domain THz fields as $R = |r|^2 = |E_{reflected,sample}(\omega)/E_{reflected,gold}(\omega)|^2$.

Linear reflectivities were recorded at the lowest achievable field strengths while nonlinear reflectivities were taken at higher field strengths (20 kV/cm < E < 80 kV/cm). Incident pulses with central frequency of ω_{pump}=0.45 THz was used for the measurements in x=9.5% and 11.5% doping. The "weight" of the third harmonic component in the nonlinear reflectivity (800 GHz and 1.5 THz, red and blue shaded regions in figure 2 and 4 in main text), therefore could be obtained by subtracting normalized linear reflected electric field (with gold) taken at low fields from the normalized nonlinear electric field taken at high fields (i.e. the integrated $r_{nonlinear} - r_{linear} = \frac{E_{sample,nonlinear}}{E_{gold,nonlinear}} - \frac{E_{sample,linear}}{E_{gold,linear}}$ in the frequency range between 800 GHz and 1.5 THz). Note that for the x=15.5% sample in order to obtain a clear third harmonic signal without interference from the reflectivity edge at the plasma frequency (1.4 THz), THz

pulses with ω_{pump}=0.7 THz, was used. Hence for this case, a similar procedure explained earlier was used, albeit for the frequency range 1.7 THz-2.3 THz. The THz field transient and the corresponding spectrum was to obtain the measurements are shown in Section S3.

Equivalent results were obtained by subtracting the reflected *high field* signal at high temperatures (field-independent) from that measured in the reported ranges (field-dependent).(i.e. the integrated $E_{sample,T} - E_{sample,T \gg T_{CO}} \propto r_T - r_{T \gg T_{CO}}$, where $r_{T \gg T_{CO}}$ is field-independent) .
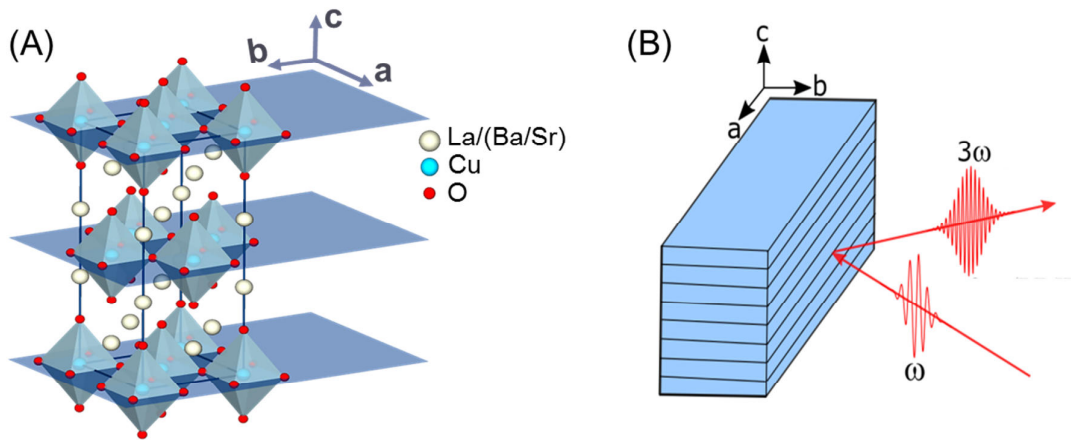

Figure S1 – (A) Schematic crystal structure of La$_{2-x}$Ba$_x$CuO$_4$ indicating the *c* axis stacked Cu-O planes. (B) Schematic representation of the experimental geometry.

S2: Linear optical properties of La$_{2-x}$Ba$_x$CuO$_4$ - x=9.5% & x=11.5%

As shown in Fig. S2, the linear reflectivity of the x=9.5% sample shown in Fig. S1 displays a temperature dependent red shift of the Josephson plasma resonance.

The corresponding imaginary part of the optical conductivity, $\sigma_2(\omega)$, is also displayed. This was determined by Kramers-Kronig transformation, after merging the THz frequency reflectivity data reported here with the high frequency spectra reported in the literature for the same batch of samples(7). The superfluid density $\omega\sigma_2(\sigma \to 0)$ plotted in Fig. 2 was computed from the data shown here.
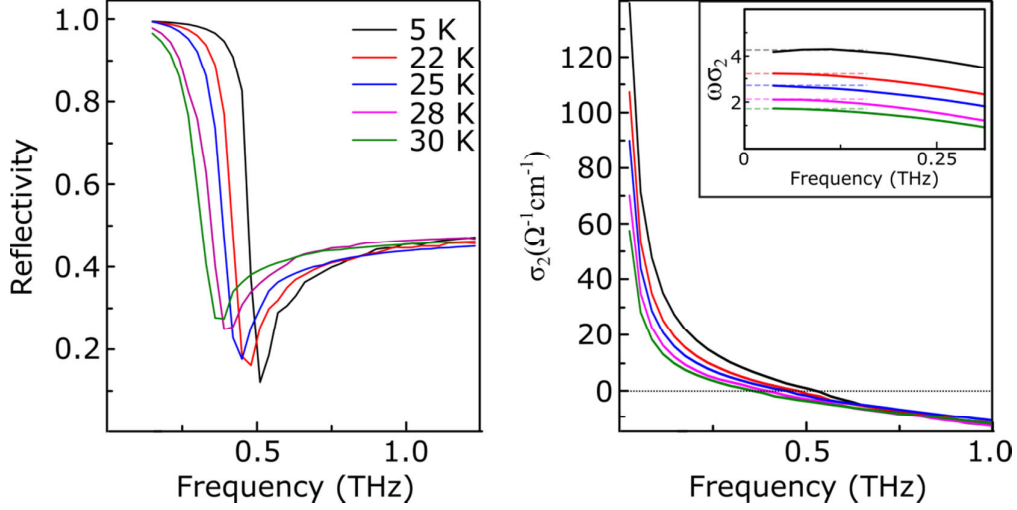
Figure S2 – (A) Temperature dependent reflectivity of x=9.5% doped sample measured in the linear regime (i.e. E=8kV/cm) (B) The corresponding σ_2 extracted through a Kramers-Kronig transformation. The superfluid density $\omega\sigma_2(\sigma \to 0)$ is shown in the inset.

The THz reflectivity of the x=11.5% sample in the linear regime, measured in a different experimental setup (based on a photoconductive antenna for THz generation) is shown in Fig. S3. We find indications of a Josephson Plasma edge at approximately 150 GHz(*29*). This feature is observed to disappear as T approaches T_c=13 K.
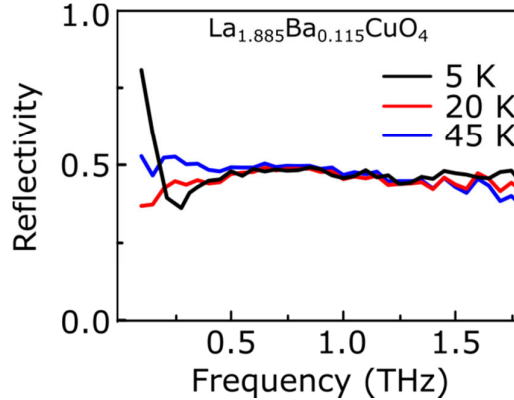

Figure S3: THz reflectivity in the linear regime of x=11.5% sample.

S3: Simulation of the nonlinear optical properties from the sine-Gordon equation

A Josephson junction with semi-infinite layers stacked along the *z* direction (with translational invariance along the *y* direction) was modeled with the one-dimensional sine-Gordon equation(*16*, *17*). The Josephson phase evolution in each stack $\theta_{i,i+1}(x,t)$, (with x being the propagation direction) is described by:

$$\frac{\partial^2 \theta_{i,i+1}(x,t)}{\partial x^2} - \frac{1}{\gamma}\frac{\partial \theta_{i,i+1}(x,t)}{\partial t} - \frac{\varepsilon_r}{c^2}\frac{\partial^2 \theta_{i,i+1}(x,t)}{\partial t^2} = \frac{\omega_{JP0}^2 \varepsilon_r}{c^2}\sin\theta_{i,i+1}(x,t) \qquad \text{(S1)}$$

The damping factor γ is a fitting parameter used to reproduce the experimental observations. For simplicity, *i.e.* we redefine $\theta_{i,i+1}(x,t) = \theta(x,t)$.

The Josephson phase evolution and the reflected field (E_r) are computed through the sine-Gordon equation along with the following boundary conditions at the vacuum-sample interface(*12, 14*).

$$[E_i(t) + E_r(t)]_{x=-0} = E_c(x,t)|_{x=+0} = H_0 \frac{1}{\omega_{JP0}\sqrt{\varepsilon}}\frac{\partial \theta(x,t)}{\partial t}|_{x=+0}, \qquad \text{(S2)}$$

$$[H_i(t) + H_r(t)]_{x=-0} = H_c(x,t)|_{x=+0} = -H_0\lambda_J \frac{\partial \theta(x,t)}{\partial x}|_{x=+0}. \qquad \text{(S3)}$$

Here E_c denotes the field propagating inside the superconducting cuprate, $H_0 = \Phi_0/2\pi D\lambda_J$, where Φ_0 is the flux quantum $\left(\Phi_0 = \frac{hc}{2e}\right)$, λ_J is the field penetration depth and D is the distance between adjacent superconducting layers. The equilibrium Josephson Plasma Resonance is an input parameter in the simulations, which is chosen to be that measured in linear spectrum, *i.e.* $\omega_{JP0} = 0.5$ THz and $\omega_{JP0} = 1.4$ THz for x=9.5% and 15.5% doping, respectively.

The THz field impinging (E_i) on the superconductor at the boundary $x = 0$ was taken as the digitized experimental field reflected from the gold reference, E_{gold} (Fig. S4). For fields in vacuum ($x < 0$), the Maxwell's equations imply

$$E_i - E_r = \frac{\omega\mu}{ck}(H_i + H_r) = H_i + H_r . \qquad \text{(S4)}$$

By combining Eq. (S3) with Eq. (S1) and (S2) we obtain the boundary condition

$$\frac{2\sqrt{\varepsilon}}{H_0}E_i(t)|_{x=-0} = \frac{\partial \theta(x,t)}{\omega_{JPR}\partial t}|_{x=+0} - \sqrt{\varepsilon}\frac{\partial \theta(x,t)}{\partial x/\lambda_J}|_{x=+0}. \qquad \text{(S5)}$$

After solving the Josephson phase through Eq. (S1) and Eq. (S5), the reflected field is obtained from Eq. (S4). The reflectivity is then computed as the ratio between the Fourier transforms of the reflected field and the input field as

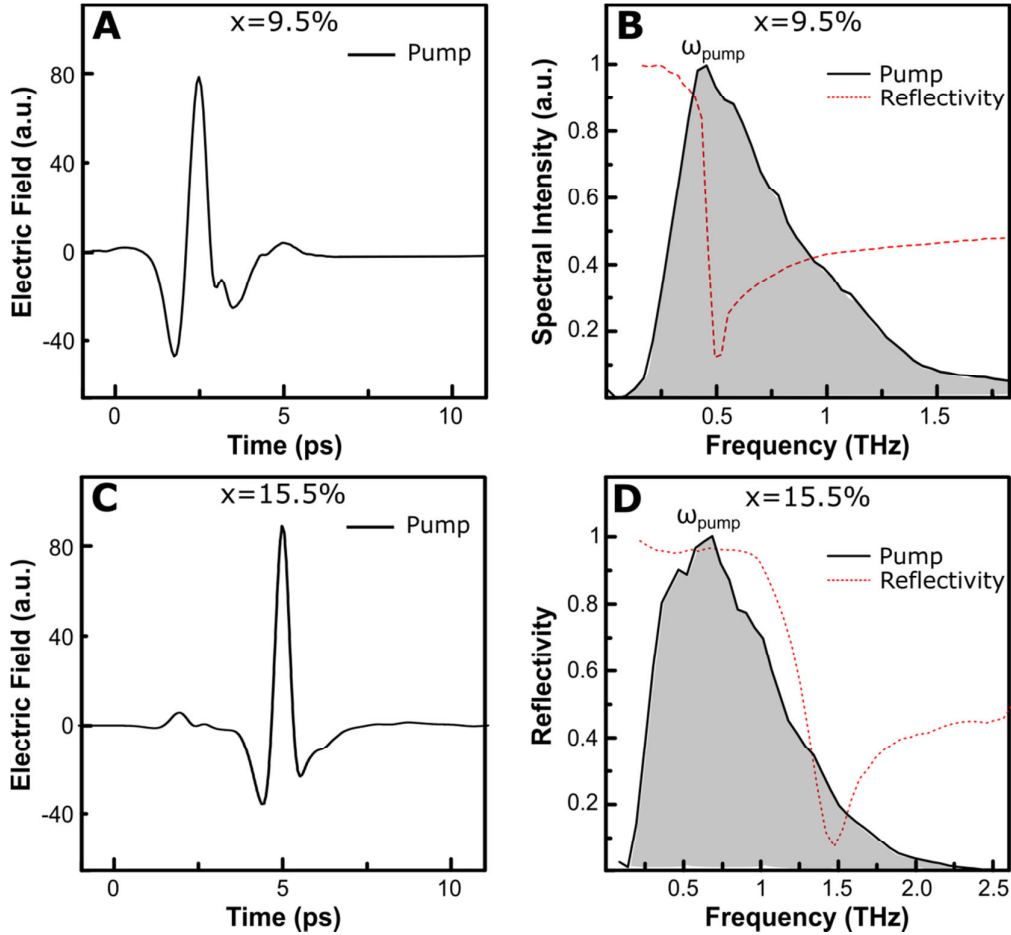$$R(\omega) = |E_r(\omega)/E_i(\omega)|^2 .$$

 Figure S4 – (A) The incident THz field in time domain and (B) its frequency spectrum for the experiments on x=9.5% doping. The linear reflectivity of the sample at T=5 K is also shown. (C-D) The corresponding THz fields used for x=15.5% doping.

S4: Third Harmonic generation with frequency filtered pulses

The nature of the third harmonic generation in the bulk superconducting state was further investigated using THz pulses that were filtered to less than 10%. Intense half cycle THz pulses, generated from optical rectification in $LiNbO_3$ using tilted pulse front technique (*8*), were shaped to narrow band multi-cycle pulses, with central frequency of ω_{pump}~0.5 THz, by utilizing commercial frequency filters. These pulses had maximum field strengths of ~15 kV/cm and could therefore only be used to repeat a fraction of the experiments reported in the main text.

In Fig. S5A we show the frequency spectrum of the incident and the reflected THz pulses from the x=9.5% sample at T=5 K. In the reflected spectrum, a dip at 0.5 THz is observed, which corresponds to the Josephson Plasma Edge. In addition, a peak is observed at ~1.4 THz (inset), which corresponds to the third harmonic of the incident frequency. This feature is

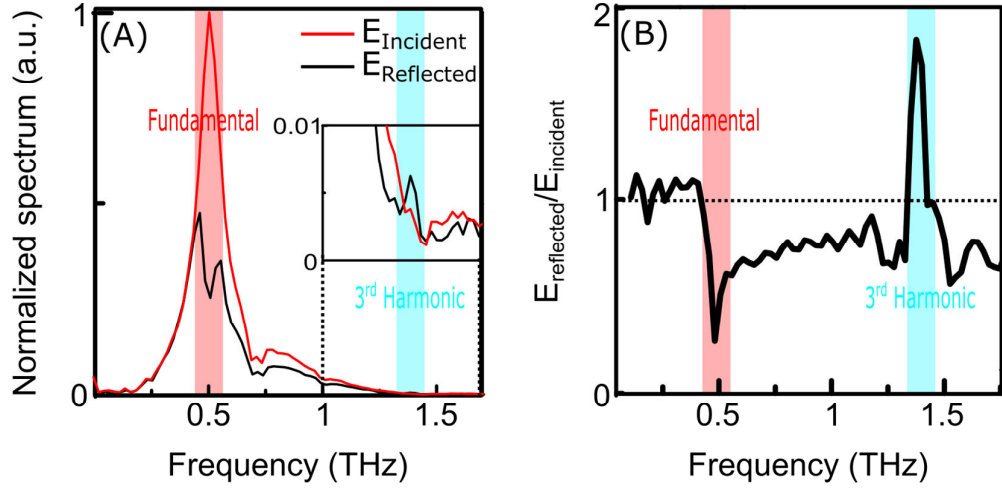clearly captured by dividing the Fourier transform of the reflected field by the incident field (Fig. S5B).

Figure S5 – (A) Fourier transforms of the incident and reflected THz fields from the x=9.5% sample at T=5 K. The inset shows a zoom in the 1 THz -1.8 THz frequency range. (B) Corresponding ratio $E_{reflected}/E_{incident}$ evidencing a third harmonic peak at ~1.4 THz.

S5: Nonlinear response of Pair Density Wave – Two π/2 Josephson Junction model

In this section, we describe the two-site model which was utilized to compute the nonlinear response of the pair density wave (PDW). Such a PDW state could be modeled as a three dimensional array of Josephson junctions(18) (represented in Fig. S6). The total energy of such Josephson junctions with the intra-stripe, inter-stripe, and inter-layer couplings J, J' and J'' could be written as

$$E_{total} = \sum_{x,y} -J\cos\left(\theta_{x,y}^1 - \theta_{x,y+1}^1\right) + J'\cos\left(\theta_{x,y}^1 - \theta_{x+1,y}^1\right) - J\cos\left(\theta_{x,y}^2 - \theta_{x+1,y}^2\right) +$$
$$J'\cos\left(\theta_{x,y}^2 - \theta_{x,y+1}^2\right) - J''\cos\left(\theta_{x,y}^1 - \theta_{x,y}^2\right) - Un_{x,y}^1 n_{x,y}^2,$$

where $\theta_{x,y}^1$ and $n_{x,y}^1$ are the superconducting phase and the charge at site (x,y) in i^{th} layer and U is the inter-layer capacitive energy. Usually $J \sim J' \gg J''$ and for the case $J'' = 0$, the ground state minimizing this energy is indeed a stripe phase configuration with $\widetilde{\theta_{x,y}^1} = \left(x + \frac{1}{2}\right)\pi$ and $\widetilde{\theta_{x,y}^2} = y\pi$.

In the following we assume $J = J' = J_0$ and for simplicity we consider two $\pi/2$ Josephson Junctions at sites $r = 1, 2$ (four lattice points). In order to study the fluctuation dynamics induced by the external driving $E(t)$, we expand the phases at each lattice point around the stripe order as $\theta_r^i = \widetilde{\theta_r^i} + \delta\theta_r^i$ where i represents the layer index. The energy of the two site model is therefore:

$$E_{two-site} = -J\cos(\delta\theta_1^1 - \delta\theta_2^1) - J\cos(\delta\theta_1^2 - \delta\theta_2^2) - \sum_{r=1,2}[Un_r^1n_r^2 - (-1)^r J'' \sin(\delta\theta_r^1 - \delta\theta_r^2)].$$

We emphasize the unusual nature of the inter-layer Josephson coupling energy [the term '$J'' \sin(\delta\theta_r^1 - \delta\theta_r^2)$'], which arises due to the frustration nature of the PDW, is crucial towards observing the third harmonic nonlinearity.
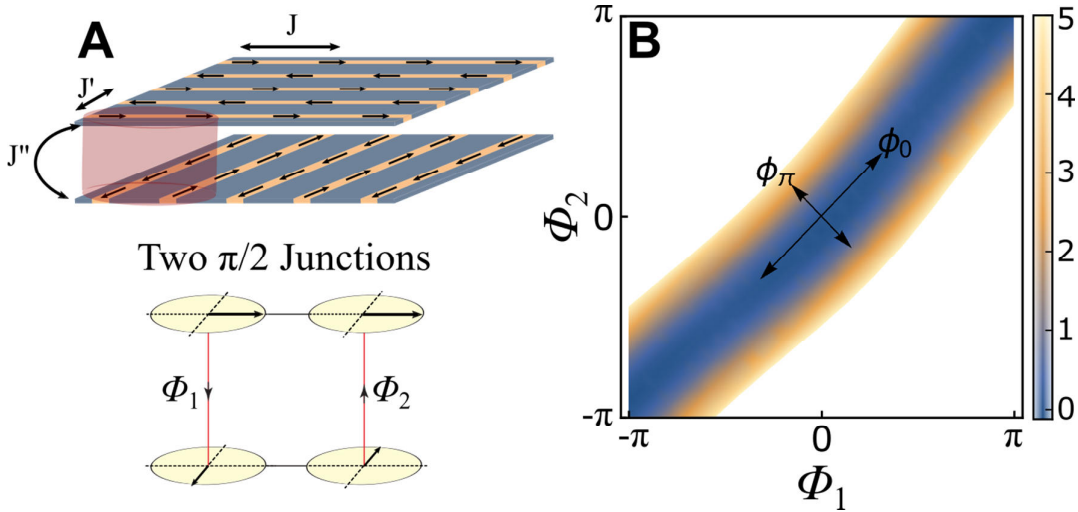

Fig. S6 – (A) Schematic representation of the Pair Density Wave and the corresponding simplified version involving two $\pi/2$ Josephson Junctions. (B) The effective potential (V_{eff}) used to simulate the nonlinear dynamics $J = 4, J'' = 0.5$ and $U = 1$.

The equation of motion of the inter-layer phase difference $\varphi_r = \delta\theta_r^1 - \delta\theta_r^2$ and its conjugate variable $(n_r^1 - n_r^2)$ are

$$\dot{\varphi}_r = \frac{\delta E_{two\,site}}{\delta n_r^1} - \frac{\delta E_{two\,site}}{\delta n_r^2} = U(n_r^1 - n_r^2),$$

$$\dot{n_r^1} - \dot{n_r^2} = -\frac{\delta E_{two-site}}{\delta(\delta\theta_r^1)} + \frac{\delta E_{two-site}}{\delta(\delta\theta_r^2)} = (-1)^r J(\varphi_1 - \varphi_2) - (-1)^r 2J'' \cos(\varphi_r),$$

where the approximation $\sin(\delta\theta_1^i - \delta\theta_2^i) \approx (\delta\theta_1^i - \delta\theta_2^i)$ was made, since the in-plane fluctuations are small due to large J. The equations of motion could be rewritten as

$$\ddot{\varphi}_1 = -UJ(\varphi_1 - \varphi_2) + 2UJ'' \cos(\varphi_1) - \gamma\dot{\varphi}_1 + F(t) \qquad (S6)$$
$$\ddot{\varphi}_2 = UJ(\varphi_1 - \varphi_2) - 2UJ'' \cos(\varphi_2) - \gamma\dot{\varphi}_2 + F(t) \qquad (S7)$$

where γ is the damping constant and $F(t)$ is a uniform external driving. For an applied electric field $E(t) = E_0\sin(\omega_{pump}t)$, $F(t) = \dot{E}(t) \sim E_0\cos(\omega_{pump}t)$

The energy conserving part of the equations can be derived from an effective potential,

$$V_{eff}(\varphi_1, \varphi_2) = \frac{UJ}{2}(\varphi_1 - \varphi_2)^2 + UJ'' \sin(\varphi_1) - UJ'' \sin(\varphi_2) \qquad (S8)$$

The first term in Eq. (S8) represents the in-plane elastic energy while the other terms represent the frustrated inter-layer Josephson energy. These terms makes the effective potential slightly curved (Fig. S6) and this result in two important features.

1) The equilibrium state is one with the phase at each lattice site has a small tilt angle $\left(\varphi_1 = -\varphi_2 \approx \frac{J''}{J}\right)$ on top of the collinear configuration.

2) In the presence of an external applied field $E(t)$, φ_1 and φ_2 is driven in-phase by $F(t) = \dot{E}(t)$, while the curved shape of the potential V_{eff} induces small out-phase motions. Such dynamics therefore confirms the existence of two collective modes $\varphi_0 = (\varphi_1 + \varphi_2)/2$ and $\varphi_\pi = (\varphi_1 - \varphi_2)/2$.

Assuming that $\varphi_0 \ll \varphi_\pi$, one could rewrite Eq. (S6) and Eq. (S7) as:

$$\ddot{\varphi}_0 = -2UJ'' \sin(\varphi_0) \sin(\varphi_\pi) - \gamma\dot{\varphi}_1 + F(t) \approx -2UJ''\varphi_0\varphi_\pi - \gamma\dot{\varphi}_0 + F(t), \qquad (S9)$$
$$\ddot{\varphi}_\pi = 2UJ'' \cos(\varphi_0) \cos(\varphi_\pi) - 2UJ\varphi_\pi - \gamma\dot{\varphi}_1 \approx 2UJ'' - 2UJ\varphi_\pi - UJ''\varphi_0^2 - \gamma\dot{\varphi}_\pi. \qquad (S10)$$

It is evident from Eq. (S9) that the applied field $E(t)$ excites φ_0. In addition to its response at the excitation frequency ω_{pump}, φ_0 undergoes plasma oscillation at $\omega_{JP0} = \sqrt{2UJ''^2/J}$. These plasma oscillations arises only when $\varphi_\pi \neq 0$.

Also, it is clear from Eq. (S10) that φ_π is excited only through φ_0^2 term, hence φ_π has a response at $2\omega_{pump}$. Therefore, in the Fourier space, we may approximate φ_0 by a single mode $\varphi_0(\omega_{pump})$. The φ_π mode may be approximated with two frequency components $\varphi_\pi(0)$ and $\varphi_\pi(2\omega_{pump})$.

Now the total current is given by

$$I(t) = J'' \cos(\varphi_1) - J'' \cos(\varphi_2) \approx -2J'' \varphi_0(t)\varphi_\pi(t) + \frac{J''}{3} \varphi_0^3(t)\varphi_\pi(t) \tag{S11}$$

In the Fourier space, the same equation reads as:

$$\begin{aligned}
I(\omega) \approx -2J'' \varphi_0(\omega_{pump})\varphi_\pi(0) + \frac{J''}{3} \varphi_0^3(\omega_{pump})\varphi_\pi(2\omega_{pump}) \\
-2J'' \varphi_0(\omega_{pump})\varphi_\pi(2\omega_{pump}) + \frac{J''}{3} \varphi_0^3(\omega_{pump})\varphi_\pi(0)
\end{aligned} \tag{S12}$$

The contributions to the third harmonic generation (current response at $3\omega_{THz}$) could be divided into two terms:

1) A term proportional to the $\varphi_0^3(\omega_{pump})\varphi_\pi(0)$. This term can exist only when $\varphi_\pi \neq 0$. Or in other words, when there is finite superfluid tunneling between the layers which occurs at $T < T_c$.

2) The term proportional to $\varphi_0(\omega_{pump})\varphi_\pi(2\omega_{pump})$ which arises from the nonlinear coupled dynamics of the PDW state. Such contributions would be present even when $\varphi_\pi = 0$ and hence could be postulated to explain the experimental observation of third harmonic generation (THG) at $T > T_c$ in the stripe ordered state.

We have numerically integrated Eq. (S6) and (S7) with an initial steady state until $t = 300$. Note that the time coordinate was normalized with ω_{pump}. The computations were performed with $J = 4$, $J'' = 0.5$, $U = 1$, $\gamma = 0.2$ and $\omega_{THz} = 1$. The parameters were chosen so as to match the experiments ($\omega_{JP0} = 0.15\ THz$, $\omega_{THz} = 0.45\ THz$, $\frac{\omega_{JP0}}{\omega_{pump}} = 0.35$). The driving is taken as $F(t) = F_0 \exp(-\frac{(t-t_E)^2}{2\Delta_E^2}) \cos(\omega_{pump}t)$ with $t_E = 100$ and $\Delta_E = 5$.

The power spectrum of the current response for driving amplitudes of $F_0 = 0.05$ and $F_0 = 0.5$ is shown in in Fig. S7. The strength of the driving amplitude corresponds to tens of kV/cm for $F_0 = 0.5$. A third harmonic response is observed for the larger amplitude of driving. Further, the contribution to the THG from the two terms discussed above is shown in Fig. S7(B). It could be noted that the significant contribution to THG arises from the novel dynamical coupling of the collective modes of the PDW. However, we note the presence of the term proportional to $\varphi_0^3(\omega_{pump})\varphi_\pi(0)$. This is due to the limitation of our model which

does not have a clear phase transition below which the static φ_π mode (the finite static tilting of the phases) vanishes ($\varphi_\pi = 0$).
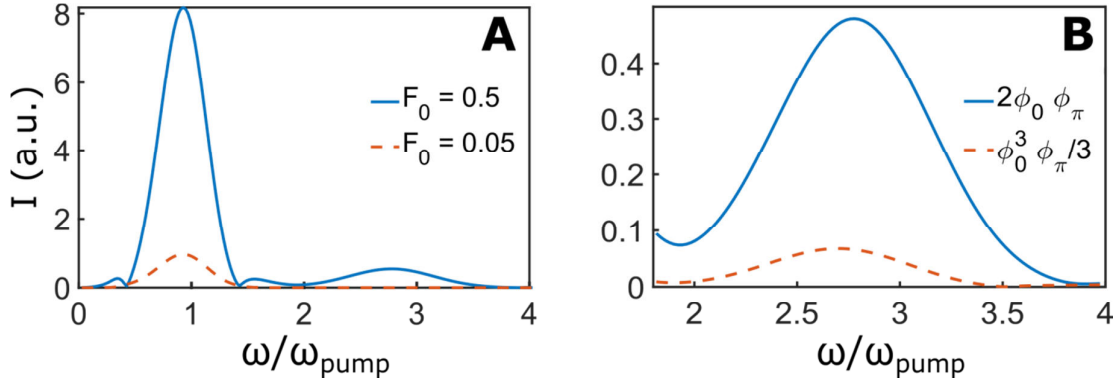

Fig. S7 – (A) The computed current response in the linear ($F_0 = 0.05$) and nonlinear ($F_0 = 0.5$) regimes. A clear response at the third harmonic of the driving field is observed in the nonlinear excitation regime. (B) The contribution of the different terms discussed in the text to the third harmonic intensity.

S6: Nonlinearities from quasiparticles –First principle DFT calculations

In this section an estimate for a second contribution to the third harmonic We quantify the third harmonic generated from the free carrier motion in the anharmonic Bloch bands. Specifically, the deviation of the band dispersion from a parabola ($\epsilon \approx a_2\, k^2 + a_4\, k^4$) results in third harmonic emission.

An applied electric field imparts a finite momentum to the free carriers, following which they explore various Bloch states while acquiring group velocities $v_g(t)$ depending on the band curvature. Radiation emerges as the charges are accelerated and hence as

$$\frac{dI_{intra}}{dt} = \frac{d}{dt}\left[n_e\, v_g(t)\right] = n_e\,\frac{dv_g(t)}{dt} \;, \tag{S13}$$

with n_e the number of mobile charge carriers within the band and $v_g(t)$ the group velocity.

To obtain the time dependent group velocity we use the known relation involving the time dependent momentum change $k(t)$ and the dispersion relation $\epsilon(\mathrm{k})$ which finally give:

$$v_g(t) = \frac{1}{\hbar}\,\frac{d\epsilon(\mathrm{k})}{d\mathrm{k}}\bigg|_{k(t)} \;. \tag{S14}$$

11

Lastly, starting from a Drude model the time dependence of the momentum ($k(t)$) is given by

$$\frac{dk(t)}{dt} = \frac{e}{\hbar} E(t) - 2\frac{k(t)}{\gamma} \quad ,$$ (S15)

with e the electron charge, E(t) the time dependent electric field and γ the mean free time of the electrons.

Experimental and material specific parameters were computed in the following fashion:

1) We computed $k(t)$ with parameters E(t) and mean free time, similar to what is observed in the experiments.
2) We performed computations of the electronic structure of $La_{1.92}Ba_{0.08}CuO_4$ (LBCO) to determine the band structure $\epsilon(k)$.
3) We combined the two steps and perform a Fast Fourier Transformation (FFT) of the resulting $dv_g(t)/dt$, which gives the spectrum of emitted light.

Since the applied THz field is polarized along the c-axis of LBCO, the free carriers would accelerate along the $\Gamma - Z$ direction parallel to the reciprocal c* vector (the Brilloun-zone of LBCO is shown in Fig. S8(A)). The k(t) for a single Gaussian pulse with $f = 0.45\,THz$, $E_{max} = 65\,kV/cm$, $FWHM = 3\,ps$ and $\gamma = 70\,fs$ was computed from Eq. (S15) (Fig. S8(B)). The resulting momentum oscillations are small with a maximum amplitude not exceeding 10% of c*. Consequently, the electron oscillations are confined close to the center of the Brillouin zone.

We compute the electronic band structure of LBCO by performing first principle computations in the framework of DFT. For our calculations, we use DFT as expanded with an augmented plane wave plus local orbital (APW+lo) basis as implemented in the ELK code(30). As approximation for the exchange correlation functional we use the generalized gradient approximation corresponding to Perdue, Burke and Ernzerhof(31) (PBE) and to improve the description of correlation effects of the Cu d-electrons we employ a DFT+U scheme(32). For the latter, we use a U=5eV and J=0 and apply the fully localized limit for the double counting correction term. As a structural input of our computations we use the data provided for LBCO in Ref [(33)] and treat the chemical doping by fractional site occupation

of La(Ba) using the virtual crystal approximation (VCA). Finally, we perform several convergence tests on the band structure of LBCO and assume convergence if $\Delta\epsilon(k) \leq 0.1 meV$, which we obtain for the numerical parameters given under Ref. [(*34*)].

Fig. S8(C) shows the dispersion of the bands in the closest vicinity of the Fermi level, two valence and one conduction band, along the $\Gamma - Z$ direction within the Brillouin zone. Please note, the large separation of the valence and conduction band in the order of $2\ eV$, which is three order of magnitude larger compared to the THz pulse frequency. Consequently, the amount of carries generated by THz field in these bands is expected to be small.
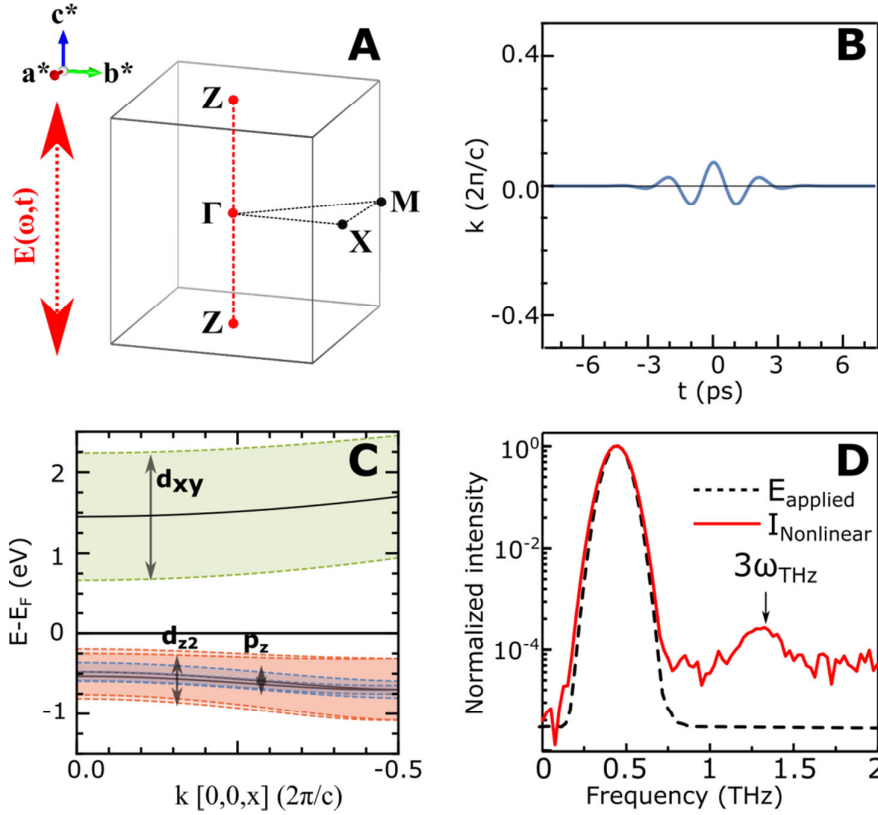

Figure S8 – (A) Brillouin Zone of LBCO x=9.5% doped sample indicating the high symmetry points. (B) The $k(t)$ excited along the Γ-Z direction by an electric field E(t), which frequency spectra is shown in (D). (C) The electronic band structure along Γ-Z direction indicating three bands (one conduction and two valence bands). The fat band color coding indicates the weighted symmetry of the bands. (D) The computed current response and applied electric pulse. The former clearly indicates a weak third harmonic contribution.

We also analyze the symmetry of the bands plot the band characters by as fatbands plot in Fig. S8(C). The character of conduction band is d_{xy} whereas the valence bands exhibit a combination of $d_{z^2} + p_z$. Considering, in this respect the dipole transition matrix elements between these bands we find them vanishing since the combination of symmetries does not obey the dipole transition rules ($\Delta l = 1, \Delta m = 0, \pm 1$). Consequently, beside the large energy separation also band character strongly suppresses transitions and the generation of movable

charge carriers. Note that also indirect tunneling transitions, which are according Ref. [(*21*)] given by the square of the dipole transition matrix elements, become strongly suppressed. Consequently, even without explicitly computing the quantitate amount of carriers we anticipate a negligible amount of total emitted harmonics.

Independent of the only small amount of available charge carriers we compute the relative magnitude of the third harmonic generated light by evaluating Eq. (S13) after fitting the dispersion relation with a polynomial expression. We further sum the contribution of from the three bands considering the same electron/hole content in each. The resulting emitted light spectrum after the FFT is displayed in Fig. S8(D). We find a strong component at the fundamental, whereas the third harmonic component is 3-4 orders of magnitude smaller. Please, note that increasing the amount of charge carriers will leave the relative size of the generated light unchanged since n_e equally scales all components independent of the frequency.

S7: Nonlinearities from charge order – Negligible contribution

In this section we present our argument against the charge density wave (CDW) as the cause of the observed nonlinearities. Although de-pinning a charge density wave can, in principle, generate radiation at the Third-Harmonic (*22*), we show here that it is highly unlikely under the experimental conditions.

The frequency dependence of the cubic dielectric constant for a sliding CDW scales as $\epsilon^{(3)} \sim E_{inc}^2 \omega_{inc}^{-5}$, where E_{inc} and ω_{inc} are the field strength and the frequency of the applied electric field (*22*). Starting from this formula, even considering the larger fields used in our experiment (100 kV/cm in the present work vs V/cm in Ref. (*22*)) and considering the appropriate frequency difference (0.5 THz in the present work vs 1 Hz - 8 KHz in Ref. (*22*)), one finds that the Third Harmonic from a CDW should be atleast thirteen orders of magnitude weaker in our experiment.

Physically, this is understood by considering that the total kinetic energy acquired by a confined particle in an electromagnetic field scales with $1/\omega^2$. Hence, the velocity of a charged particle is between sixteen and twenty orders of magnitude larger at 10 KHz and 1Hz than at 1 THz. The lower energy results in a smaller cubic anharmonicities and explains the difference discussed above.

References and Notes

1. M. Hücker, M. v. Zimmermann, G. D. Gu, Z. J. Xu, J. S. Wen, G. Xu, H. J. Kang, A. Zheludev, J. M. Tranquada, Stripe order in superconducting $La_{2-x}Ba_xCuO_4$ ($0.095 < x < 0.155$). *Phys. Rev. B* **83**, 104506 (2011). doi:10.1103/PhysRevB.83.104506

2. P. Abbamonte, A. Rusydi, S. Smadici, G. D. Gu, G. A. Sawatzky, D. L. Feng, Spatially modulated "Mottness" in $La_{2-x}Ba_xCuO_4$. *Nat. Phys.* **1**, 155–158 (2005). doi:10.1038/nphys178

3. J. M. Tranquada, B. J. Sternlieb, J. D. Axe, Y. Nakamura, S. Uchida, Evidence for stripe correlations of spins and holes in copper oxide superconductors. *Nature* **375**, 561–563 (1995). doi:10.1038/375561a0

4. Q. Li, M. Hücker, G. D. Gu, A. M. Tsvelik, J. M. Tranquada, Two-dimensional superconducting fluctuations in stripe-ordered $La_{1.875}Ba_{0.125}CuO_4$. *Phys. Rev. Lett.* **99**, 067001 (2007). doi:10.1103/PhysRevLett.99.067001 Medline

5. E. Berg, E. Fradkin, E.-A. Kim, S. A. Kivelson, V. Oganesyan, J. M. Tranquada, S. C. Zhang, Dynamical layer decoupling in a stripe-ordered high-T_c superconductor. *Phys. Rev. Lett.* **99**, 127003 (2007). doi:10.1103/PhysRevLett.99.127003 Medline

6. M. H. Hamidian, S. D. Edkins, S. H. Joo, A. Kostin, H. Eisaki, S. Uchida, M. J. Lawler, E.-A. Kim, A. P. Mackenzie, K. Fujita, J. Lee, J. C. S. Davis, Detection of a Cooper-pair density wave in $Bi_2Sr_2CaCu_2O_{8+x}$. *Nature* **532**, 343–347 (2016). doi:10.1038/nature17411 Medline

7. C. C. Homes, M. Hücker, Q. Li, Z. J. Xu, J. S. Wen, G. D. Gu, J. M. Tranquada, Determination of the optical properties of $La_{2-x}Ba_xCuO_4$ for several dopings, including the anomalous $x = 1/8$ phase. *Phys. Rev. B* **85**, 134510 (2012). doi:10.1103/PhysRevB.85.134510

8. J. Hebling, K.-L. Yeh, M. C. Hoffmann, B. Bartal, K. A. Nelson, Generation of high-power terahertz pulses by tilted-pulse-front excitation and their application possibilities. *J. Opt. Soc. Am. B* **25**, B6 (2008). doi:10.1364/JOSAB.25.0000B6

9. Materials and methods are available as supplementary materials.

10. Y. Laplace, A. Cavalleri, Josephson plasmonics in layered superconductors. *Adv. Phys. X* **1**, 387–411 (2016). doi:10.1080/23746149.2016.1212671

11. A. Dienst, M. C. Hoffmann, D. Fausti, J. C. Petersen, S. Pyon, T. Takayama, H. Takagi, A. Cavalleri, Bi-directional ultrafast electric-field gating of interlayer charge transport in a cuprate superconductor. *Nat. Photonics* **5**, 485–488 (2011). doi:10.1038/nphoton.2011.124

12. A. Dienst, E. Casandruc, D. Fausti, L. Zhang, M. Eckstein, M. Hoffmann, V. Khanna, N. Dean, M. Gensch, S. Winnerl, W. Seidel, S. Pyon, T. Takayama, H. Takagi, A. Cavalleri, Optical excitation of Josephson plasma solitons in a cuprate superconductor. *Nat. Mater.* **12**, 535–541 (2013). doi:10.1038/nmat3580 Medline

13. (1) In addition to the two features, a reflectivity spike at ω_{JP0} is observed for $x = 9.5\%$ doping. This feature corresponds to a parametric amplification of the Josephson plasma waves [see (*14*)]. (2) The central frequency of the terahertz pulses for experiments in $x = 9.5$ and 11.5% was $\omega_{pump} = 0.45$ THz. Note that to obtain a clear third-harmonic signal without interference from the reflectivity edge at the plasma frequency in $x = 15.5\%$ sample, terahertz pulses with $\omega_{pump} = 0.7$ THz were used.

14. S. Rajasekaran, E. Casandruc, Y. Laplace, D. Nicoletti, G. D. Gu, S. R. Clark, D. Jaksch, A. Cavalleri, Parametric amplification of a superconducting plasma wave. *Nat. Phys.* **12**, 1012–1016 (2016). doi:10.1038/nphys3819 Medline

15. B. D. Josephson, Coupled superconductors. *Rev. Mod. Phys.* **36**, 216–220 (1964). doi:10.1103/RevModPhys.36.216

16. S. Savel'ev, V. A. Yampol'skii, A. L. Rakhmanov, F. Nori, Terahertz Josephson plasma waves in layered superconductors: Spectrum, generation, nonlinear and quantum phenomena. *Rep. Prog. Phys.* **73**, 026501 (2010). doi:10.1088/0034-4885/73/2/026501

17. X. Hu, S.-Z. Lin, Phase dynamics in a stack of inductively coupled intrinsic Josephson junctions and terahertz electromagnetic radiation. *Supercond. Sci. Technol.* **23**, 053001 (2010). doi:10.1088/0953-2048/23/5/053001

18. E. Berg, E. Fradkin, S. A. Kivelson, J. M. Tranquada, Striped superconductors: How spin, charge and superconducting orders intertwine in the cuprates. *New J. Phys.* **11**, 115004 (2009). doi:10.1088/1367-2630/11/11/115004

19. R. W. Boyd, Z. Shi, I. De Leon, The third-order nonlinear optical susceptibility of gold. *Opt. Commun.* **326**, 74–79 (2014). doi:10.1016/j.optcom.2014.03.005

20. B. Buchalter, G. R. Meredith, Third-order optical susceptibility of glasses determined by third harmonic generation. *Appl. Opt.* **21**, 3221–3224 (1982). doi:10.1364/AO.21.003221 Medline

21. O. Schubert, M. Hohenleutner, F. Langer, B. Urbanek, C. Lange, U. Huttner, D. Golde, T. Meier, M. Kira, S. W. Koch, R. Huber, Sub-cycle control of terahertz high-harmonic generation by dynamical Bloch oscillations. *Nat. Photonics* **8**, 119–123 (2014). doi:10.1038/nphoton.2013.349

22. T. Chen, L. Mihály, G. Grüner, Nonlinear ac dynamics of pinned charge-density waves: Third-harmonic generation. *Phys. Rev. B Condens. Matter* **36**, 2931–2934 (1987). doi:10.1103/PhysRevB.36.2931 Medline

23. G. Ghiringhelli, M. Le Tacon, M. Minola, S. Blanco-Canosa, C. Mazzoli, N. B. Brookes, G. M. De Luca, A. Frano, D. G. Hawthorn, F. He, T. Loew, M. Moretti Sala, D. C. Peets, M. Salluzzo, E. Schierle, R. Sutarto, G. A. Sawatzky, E. Weschke, B. Keimer, L. Braicovich, Long-range incommensurate charge fluctuations in $(Y,Nd)Ba_2Cu_3O_{6+x}$. *Science* **337**, 821–825 (2012). doi:10.1126/science.1223532 Medline

24. J. Chang, E. Blackburn, A. T. Holmes, N. B. Christensen, J. Larsen, J. Mesot, R. Liang, D. A. Bonn, W. N. Hardy, A. Watenphul, M. Zimmermann, E. M. Forgan, S. M. Hayden, Direct observation of competition between superconductivity and charge density wave order in $YBa_2Cu_3O_{6.67}$. *Nat. Phys.* **8**, 871–876 (2012). doi:10.1038/nphys2456

25. J. Corson, R. Mallozzi, J. Orenstein, J. N. Eckstein, I. Bozovic, Vanishing of phase coherence in underdoped $Bi_2Sr_2CaCu_2O_{8+\delta}$. *Nature* **398**, 221–223 (1999). doi:10.1038/18402

26. L. S. Bilbro, R. V. Aguilar, G. Logvenov, O. Pelleg, I. Božović, N. P. Armitage, Temporal correlations of superconductivity above the transition temperature in $La_{2−x}Sr_xCuO_4$ probed by terahertz spectroscopy. *Nat. Phys.* **7**, 298–302 (2011). doi:10.1038/nphys1912

27. K. Fujita, M. H. Hamidian, S. D. Edkins, C. K. Kim, Y. Kohsaka, M. Azuma, M. Takano, H. Takagi, H. Eisaki, S. Uchida, A. Allais, M. J. Lawler, E.-A. Kim, S. Sachdev, J. C. S. Davis, Direct phase-sensitive identification of a *d*-form factor density wave in

underdoped cuprates. *Proc. Natl. Acad. Sci. U.S.A.* **111**, E3026–E3032 (2014). doi:10.1073/pnas.1406297111 Medline

28. P. A. Lee, Amperean pairing and the pseudogap phase of cuprate superconductors. *Phys. Rev. X* **4**, 031017 (2014). doi:10.1103/PhysRevX.4.031017

29. D. Nicoletti, E. Casandruc, Y. Laplace, V. Khanna, C. R. Hunt, S. Kaiser, S. S. Dhesi, G. D. Gu, J. P. Hill, A. Cavalleri, Optically induced superconductivity in striped $La_{2-x}Ba_xCuO_4$ by polarization-selective excitation in the near infrared. *Phys. Rev. B* **90**, 100503 (2014). doi:10.1103/PhysRevB.90.100503

30. The Elk FP-LAPW Code; http://elk.sourceforge.net/.

31. J. P. Perdew, K. Burke, M. Ernzerhof, Generalized gradient approximation made simple. *Phys. Rev. Lett.* **77**, 3865–3868 (1996). doi:10.1103/PhysRevLett.77.3865 Medline

32. V. I. Anisimov, F. Aryasetiawan, A. I. Lichtenstein, First-principles calculations of the electronic structure and spectra of strongly correlated systems: The LDA+*U* method. *J. Phys. Condens. Matter* **9**, 767–808 (1997). doi:10.1088/0953-8984/9/4/002

33. S. Katano, J. A. Fernandez-Baca, S. Funahashi, N. Môri, Y. Ueda, K. Koga, Crystal structure and superconductivity of $La_{2-x}Ba_xCuO_4$ ($0.03 \leq x \leq 0.24$). *Physica C* **214**, 64–72 (1993). doi:10.1016/0921-4534(93)90108-3

34. For the self-consistent computations, we sample the Brillouin zone with a *k* point mesh of 15 by 15 by 7, set the angular momentum truncation of the potential and wave function inside the muffin tins to $l_{max(APW)} = 12$ and set the product of the average muffin tin radius and the maximum reciprocal lattice vector to be 7.5 (APW, augmented plane method). Moreover, we set the number of empty states to 15 for each atom within the unit cell. The self-consistent calculations are reiterated until the root mean square change of the potential and the total energy becomes smaller than 10^{-7} and 10^{-8} Hartree, respectively. Finally, we determine the band structure from non–self-consistent calculations using the previous converged potentials and a fine *k* point mesh grid of 600 *k* points along the *c** direction.